Magnetic Interactions at Optical Frequencies in an InP-Based Waveguide Device with Metamaterial

Tomohiro Amemiya, *Member, IEEE*, Takahiko Shindo, *Student Member, IEEE*, Daisuke Takahashi, Nobuhiko Nishiyama, *Senior Member, IEEE*, and Shigehisa Arai, *Fellow, IEEE*

***Abstract*— We have fabricated a novel InP-based multimode interferometer combined with a metamaterial. It consists of an array of extremely small metal split-ring resonators attached to the waveguide. In this manner, we have demonstrated magnetic interactions between the metamaterial and light traveling in the device, the device was designed for use at 1.55 μm wavelength. The transmission characteristics of the device strongly depend on the polarization and wavelength of the input light. Our results show a strong possibility of creating novel semiconductor devices, i.e., meta-photonic integrated circuits.**

***Index Terms*— Integrated optics, metamaterial, multimode interferometer, optical waveguide, photonic integrated circuit, split-ring resonator.**

I. Introduction

THE relative permeability of every natural material is 1 at optical frequencies because the magnetization of natural materials does not follow the alternating magnetic field of light. If we can overcome this restriction and control both the permeability and the permittivity at optical frequencies, we will be able to establish a new field involving optical/photonic devices for future communication technologies. In this paper, we move one step closer to this goal—we demonstrate that in photonic devices, the relative permeability can be controlled by adopting metamaterials.

Metamaterials are artificial materials designed to have permittivity and permeability values that are not possible in nature [1]–[4]. They have recently attracted considerable interest because they exhibit unusual properties such as negative refractive indexes and have potential for unique applications such as high-resolution superlenses and invisibility cloaking devices.

It is a challenging task to introduce the concept of metamaterials to semiconductor-based photonic devices (see [5]–[10] for ordinary photonic devices). We hope to apply metamaterials to realize novel optical functionalities that can potentially establish a new field, *meta-photonics*. Some novel optical functionalities have been realized previously; for example, it has been shown that in theory, it is possible to achieve sophisticated manipulation of light such as slowing, trapping, and storing of light signals in optical waveguides [11]–[16].

The key is to create optical metamaterials that can be used to control permeability and obtain *non-unity* values at optical frequencies (note that, on the other hand, permittivity can be controlled more easily than permeability). A promising method for controlling permeability involves the use of a split-ring resonator (SRR). An SRR produces a circular current in response to an incident magnetic flux, thereby producing its own flux to enhance or oppose the incident field. Consequently, an array of extremely small SRRs operates as a metamaterial layer with non-unity permeability [17]–[21]. The SRR has a simple structure that can be made sufficiently small for use at optical frequencies. Several SRR arrays exhibiting negative permeability at optical frequencies have been fabricated previously on glass substrates.

In this paper, the feasibility of employing semiconductor-based photonic devices combined with SRR-based metamaterials is examined both theoretically and experimentally. We took up the multimode- interferometer (MMI) as an example of photonic devices. First, theoretical investigations of the device structures of the SRRs and a MMI for use in the 1.5-μm-wavelength region are given in Section II. The device structure and its fabrication processes are then explained in Section III. The operating characteristics of the device, i.e., the transmission dependences on the polarization and wavelength of incident light, are given in Section IV. The magnetic resonance (and therefore, the non-unity permeability) at optical frequencies has been demonstrated for the first time, to our knowledge, by adopting a metamaterial that is attached to a semiconductor MMI. Finally, Section V concludes the paper.

II. Multimode-Interferometer with Metamaterial: Device Structure

Our metamaterial MMI device is shown in Fig. 1. It consists of a waveguide-based GaInAsP/InP 1×1 MMI on which a gold SRR array is attached. If transverse electric (TE)-mode input light for the MMI has a frequency close to the SRR-resonant frequency, magnetic interactions occur between the TE light and SRR array. Therefore, the real part of the

Manuscript received September 27, 2010; revised January 5, 2011; accepted January 17, 2011. Date of current version April 8, 2011. This work was supported in part by the Grant-in-Aid for Scientific Research, Ministry of Education, Culture, Sports, Science and Technology, Japan, under Grant 19002009, Grant 19686023, and Grant 21860031.

T. Amemiya and S. Arai are with the Quantum Nanoelectronics Research Center, Tokyo Institute of Technology, Tokyo 152-8552, Japan (e-mail: amemiya.t.ab@m.titech.ac.jp, arai@pe.titech.ac.jp).

T. Shindo, D. Takahashi, and N. Nishiyama are with the Department of Electrical and Electronic Engineering, Tokyo Institute of Technology, Tokyo 152-8552, Japan (e-mail: shindou.t.aa@m.titech.ac.jp; takahashi.d.aa@m.titech.ac.jp; n-nishi@pe.titech.ac.jp;).

Color versions of one or more of the figures in this paper are available online at http://ieeexplore.ieee.org.

Digital Object Identifier 10.1109/JQE.2011.2108268

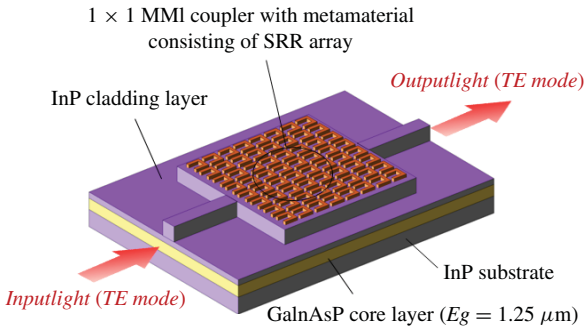

Fig. 1. GaInAsP/InP 1 × 1 multimode-interferometer (MMI) with a gold split-ring-resonator (SRR) array attached to the waveguide.

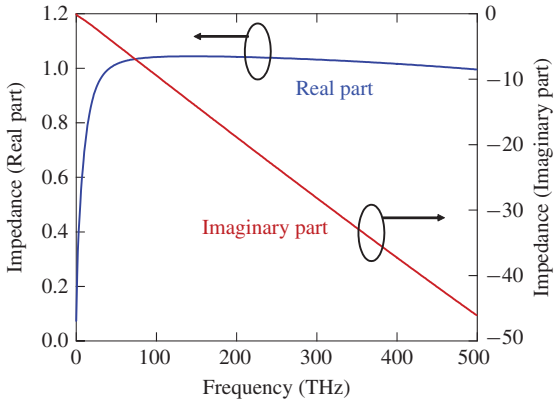

Fig. 2. Internal impedance of gold as a function of frequency (real part is surface resistivity and imaginary part is internal reactance).

macroscopic permeability becomes large positive and negative at frequencies below and above SRR resonance, respectively. Consequently, the SRR array operates as a metamaterial layer to control permeability. The imaginary part of the permeability is not 0 but a finite value under this condition (this causes the absorption loss of light).

We now investigate the optimal structure of a four-cut SRR device for use at an optical frequency of 193 THz (corresponding to 1.55 μm wavelength for low-loss optical fiber communications). The transmission characteristics are obtained by considering the magnetic interactions between the SRRs and light traveling in the MMI.

A. Design of SRR Structure for Optical Frequency

We must first determine the optimal dimensions of the SRR for the 1.5-μm-band frequency. Because the magnetic response of an SRR strongly depends on the conduction characteristics of the metal that forms the SRR, the dispersion of the internal impedance Z of the gold used in our SRRs was calculated. The internal impedance is the ratio of the surface electric field to the total current [22], [23]. Z for a unit length and unit width of a metal plane conductor is given by

$$Z(\tau) = \left(\sigma(\omega)\int_0^{\tau} \frac{\exp[ik(\omega)z] + \exp[ik(\omega)(\tau - z)]}{1 + \exp[ik(\omega)z]} dz\right)^{-1}. \quad (1)$$

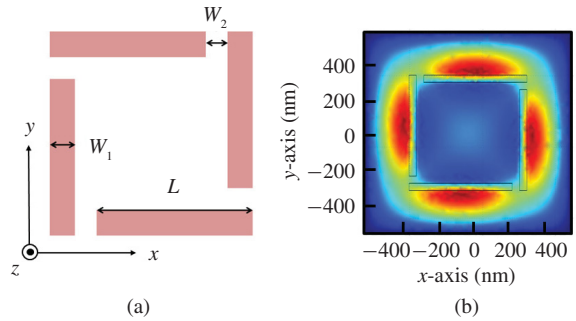

Fig. 3. Four-cut single SRR placed in air: (a) plane pattern and (b) magnetic field distribution around the SRR at resonant frequency (L = 600 nm). The distribution of field intensity is visualized by a rainbow color map.

Here, $k(\omega)$ is given by

$$k(\omega) = \omega\sqrt{\varepsilon_0\mu_0\left[1 + i\frac{\sigma(\omega)}{\omega\varepsilon_0}\right]}, \quad (2)$$

where ω is the angular frequency of light, ε_0 and μ_0 are the permittivity and permeability of vacuum, respectively, τ is the thickness of the plane conductor, and $\sigma(\omega)$ is the conductivity of the metal as defined by the Drude model.

Figure 2 shows the internal impedance as a function of frequency for a gold layer whose thickness is larger than the penetration depth. As the frequency increases, the real part of the internal impedance first increases sharply and then saturates at around 100 THz; at frequencies higher than 100 THz, it gradually decreases. This dispersion property corresponds to the dielectric behavior of gold. In contrast, the imaginary part changes monotonously with frequency and has large negative values at optical frequencies; this corresponds to ohmic losses in gold.

Using these dispersion curves, we calculated the magnetic response of a gold SRR at optical frequencies. A four-cut SRR was considered because it has high resonant frequency due to its small gap capacitance [24], [25]. The SRR was placed in a homogeneous host material (air), as shown in Fig. 3(a). If an incident AC magnetic field is applied to the SRR, an induced circular current flows in the ring through the gap capacitance. The circular current produces an internal magnetic field, and this produces a magnetic interaction between the SRR and light.

The total electromotive force (emf) induced around the SRR is given by the magnetic flux density B. Therefore, we can equate the potential drop to the emf as follows:

$$\partial_t \int_{SRR} B d\sigma = i\omega\mu_0 \int_{SRR}\left(H_{ext} + \frac{1}{4\pi}\oint \frac{j d\mathbf{s}\times\mathbf{r}}{r^3}\right) d\sigma$$
$$= V_{ring} + 4V_{gap} = \left[Z(\tau)\cdot\frac{4L}{W_1} - \frac{4W_2}{i\omega\varepsilon_0\varepsilon_m W_1\tau}\right] j. \quad (3)$$

Here, we have used Biot-Savart's law. In this equation, H_{ext} is the magnetic field of light, ε_m and $Z(\tau)$ are the relative permittivity and internal impedance of gold, respectively, τ is the thickness of the SRR, j is the induced circular current in the SRR; and L, W_1, and W_2 are the dimensions of the SRR (see Fig. 3(a)). The distribution of the magnetic field

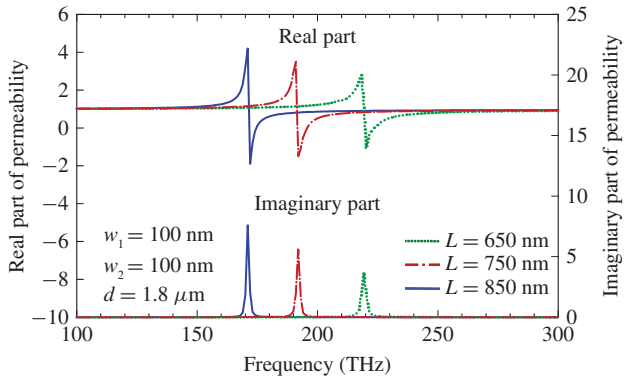

Fig. 4. Real and imaginary parts of the effective permeability of gold SRR array in air ($\varepsilon = 1$) as a function of SRR size, here, $W_1 = W_2 = 100$ nm, $d = 1.8$ μm, and frequencies = 100–300 THz.

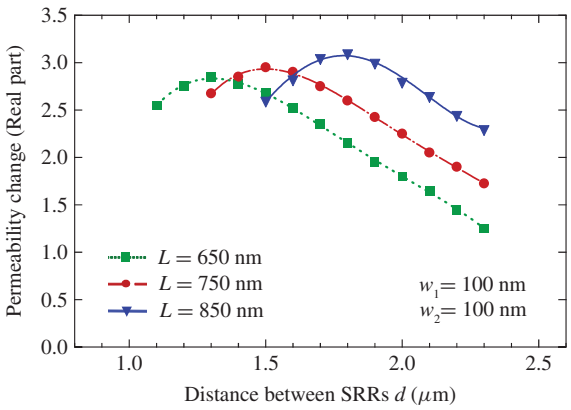

Fig. 5. Maximum change in SRR-array permeability (real part) from 1, depicted as a function of the array pitch of SRR cells. Nearest and next-nearest neighbor interactions between SRRs are considered.

around the SRR can be calculated using Eq. 3, as illustrated in Fig. 3(b).

B. Macroscopic Permeability of SRR Array

The results for a single SRR were used to calculate the effective permeability of an SRR array taking into consideration a two-dimensional array layer comprising cubic unit cells, each with an SRR at its center; both the side lengths of each cell and the array pitch of the cells were d. For simplicity, the SRRs were assumed to be placed in air. The macroscopic permeability μ_{yy} of the SRR array layer can be calculated using the field averaging equation [26], and it is given by

$$\bar{\mu}_{yy} = \frac{\bar{B}_y(0, d/2, 0)}{\bar{H}_y(0, d/2, 0)} = \mu_0 \frac{(d)^{-2} \int_{-d/2}^{d/2} dx \int_{-d/2}^{d/2} H_z(x, d/2, z) dz}{(d)^{-1} \int_0^d H_z(0, y, 0) dy}, \quad (4)$$

where B_y and H_y with over lines represent the average values of magnetic flux density and magnetic field, respectively, in the SRR array layer. To get high accuracy in this homogenization approximation, the size of the integration region should be larger than the wavelength of light. In our calculation, we therefore integrated magnetic field over a large cubic tregion that cantained a 3×3 cell array (this means that we replaced d with 3d in Eq. 4). Figure 4 shows the real and imaginary parts of permeability as a function of frequency, and the SRR size L is a parameter; here, W_1 and W_2 were set as 100 nm and d was 1.8 μm. The thickness τ of the SRR was set at twice the penetration depth of gold at each frequency. As L decreases, the magnetic resonant frequency increases. Magnetic response could be obtained at the 1.55-μm-band frequency (approximately 193 THz) for the SRR size L of 750 nm (red curves).

Further, the magnetic response of the SRR array layer depends on the array pitch d. Figure 5 shows the intensity of magnetic response, or, in other words, the maximum changes in the permeability (real part) from 1, as a function of d; L is the parameter. In this calculation, we used the nearest and next-nearest neighbor interactions between SRRs. There exists an optimal distance that maximizes the magnetic response. If d is large, the response is weak because the area density of SRRs is small; on the other hand, if d is small, the magnetic field in each SRR is canceled by the fields of the neighboring SRRs, and this weakens the total response of the SRR array layer. As L decreases, the magnetic response becomes weaker because the inductance of each SRR decreases; this increases the effective resistance (or decreases the Q factor) of the SRR.

C. Transmission Characteristics of Device

Using the abovementioned results, the transmission characteristics of an MMI with a metamaterial, which is shown in Fig. 1, were estimated using computer simulations based on the transfer-matrix method.

We first designed a device for use at 1.55-μm wavelength. The resultant structure is as follows. The substrate is an InP (refractive index $n = 3.16$). The constituent layers of the MMI are (i) a core guiding layer: 200-nm-thick $Ga_{0.25}In_{0.75}As_{0.54}P_{0.46}$ (bandgap wavelength $\lambda_g = 1.25$ μm; $n = 3.38$), (ii) InP upper cladding layer ($n = 3.16$), and (iii) SRR metamaterial layer: 50-nm-thick gold SRR array ($L = 750$ nm; $W_1 = W_2 = 100$ nm; $d = 1.6$ μm).

The thickness of the InP cladding layer affects the strength of interaction between the light traveling in the MMI and the SRR array attached to the surface of the cladding layer. Therefore, we determined the optimal thickness of the cladding layer from the following calculations.

After having designed the device structure, we calculated the transmission characteristics of the device as follows. The permeability tensor of the p-th layer, i.e., the InP substrate ($p = 1$), GaInAsP core layer ($p = 2$), InP upper cladding layer ($p = 3$), SRR array layer ($p = 4$), and air ($p = 5$), is given by

$$\tilde{\mu}_p = \begin{pmatrix} \mu_{xx}^p & 0 & 0 \\ 0 & \mu_{yy}^p & 0 \\ 0 & 0 & \mu_{zz}^p \end{pmatrix}, \quad (5)$$

where the diagonal elements μ_{xx}, μ_{yy}, and μ_{zz} are 1 at optical frequencies except in the SRR array layer. Using this tensor and the permittivity tensor ε_p for the p-th layer, Maxwell's

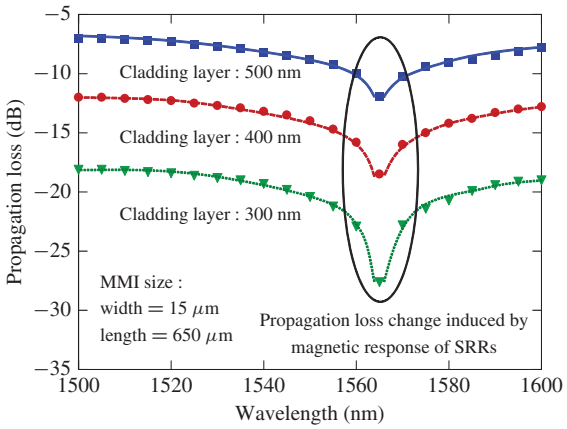

Fig. 6. Propagation loss of light in MMI with SRRs ($L = 750$ nm) as a function of wavelength, InP cladding layer thickness is a parameter. Sharp changes in propagation loss can be expected at the SRR resonance frequency.

equations are written as follows:

$$\nabla \times \mathbf{H} = j\omega\, \varepsilon_0 \tilde{\varepsilon}_p \mathbf{E}.$$
$$\nabla \times \mathbf{E} = -j\omega\mu_0 \tilde{\mu}_p \mathbf{H}. \tag{6}$$

We solved Eq. 6 under the condition that the electric and magnetic fields are invariant in the x-direction, that is, $\partial_x = 0$, and their tangential components are continuous at the boundary between the layers. For TE-mode light, the electric field E_x parallel to the z-axis is given by the following differential equation:

$$\partial_y^2 E_x + \left(k_0^2 \varepsilon_x \mu_z - \frac{\mu_z}{\mu_y}\beta^2\right) E_x = 0, \tag{7}$$

where ε_x is the diagonal element of the permittivity tensor, and $k_0 = \omega\sqrt{\mu_0\varepsilon_0} = 2\pi/\lambda$ is the free-space propagation constant. The magnetic field H_z parallel to the z-axis (propagation direction) can be calculated using E_x as follows:

$$H_z = -\frac{j}{\omega\mu_0\mu_z}\partial_y E_x. \tag{8}$$

An eigenvalue equation can be obtained using the boundary conditions with continuous E_x and H_z. In the calculations, we assumed that E_x and H_z decrease exponentially outside the GaInAsP guiding layer (i.e., in the air and the InP layers). For simplicity, we also assumed that all the layers except the SRR array layer are birefringent. The eigenvalue equation is given by

$$-\frac{j\beta_5}{\omega\mu_0\mu_z}\left(m_{11} - m_{12}\frac{j\beta_1}{\omega\mu_0\mu_z}\right) + \left(m_{21} - m_{22}\frac{j\beta_1}{\omega\mu_0\mu_z}\right) = 0, \tag{9}$$

where m_{11}–m_{22} are given by

$$\begin{bmatrix} m_{11} & m_{12} \\ m_{21} & m_{22} \end{bmatrix} = \prod_{\text{All}} \begin{bmatrix} \cosh(\beta_n d_p) & \frac{j\omega\mu_0\mu_z}{\beta_n}\sinh(\beta_n d_p) \\ \frac{\beta_n}{j\omega\mu_0\mu_z}\sinh(\beta_n d_p) & \cosh(\beta_n d_p) \end{bmatrix} \tag{10}$$

$$\beta_n = \sqrt{\frac{\mu_z}{\mu_y}\beta^2 - k_0^2\varepsilon_x\mu_z}. \tag{11}$$

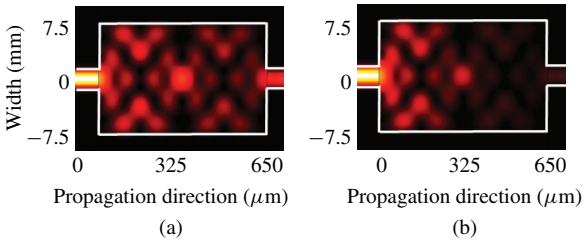

Fig. 7. Distribution profile of light traveling in metamaterial MMI device, calculated for devices with (a) *4-cut* SRR array and (b) *no-cut* gold square rings. Electric field intensity at the cross-section (x-z plane) of the device is visualized by shading. Wavelength of light is 1565 nm.

Here d_p is the thickness of the p-th layer. We solved these eigenvalue equations and obtained the effective refractive index β_n/k_0 of each layer. With these results, we calculated the transmission characteristics of the metamaterial MMI using the Fourier expansion method, which is commonly used for MMI propagation analysis [27].

Figure 6 shows the propagation loss of light traveling in the metamaterial MMI device as a function of wavelength; the InP cladding layer thickness was a parameter. A sharp change in propagation loss, therefore magnetic interaction, can be expected at the SRR resonant frequency, equivalent to 1565 nm in wavelength. A thinner cladding layer is preferable to obtain large magnetic interactions even though it increases the propagation loss because the optical field coupled to the SRR metal is larger. The light phase is shifted by the magnetic interaction, but this can be neglected compared to the effect of the abovementioned propagation loss.

Figure 7 illustrates the distribution profile of light traveling in the metamaterial MMI device. The intensity of the TE electric field at the cross-section (x-z plane) of the device is shown. The MMI is 15-μm wide, 650-μm long, and has a 450-nm-thick InP cladding layer. The wavelength of light is 1565 nm. Figure 7(a) shows our device with a *4-cut* SRR array. The light traveling in the device suffers large propagation losses because of the magnetic interactions between the SRRs and light. Figure 7(b) shows the results for a control device with *no-cut* gold square rings having the same size as a *4-cut* SRR. The *no-cut* ring has no resonant frequency and shows no magnetic interactions with 1.5-μm light; hence, the propagation loss is approximately 10 dB smaller than that of the *4-cut* SRR. These results show that the *4-cut* SRR array can successfully operate as a metamaterial layer at optical frequencies.

III. Device Fabrication

To move one step closer to the development of actual advanced optical-communication devices using the concept of metamaterials, we fabricated a trial device to confirm the magnetic response of a metamaterial comprising SRRs arrayed on a GaInAsP/InP 1 × 1 MMI coupler. The trial device was fabricated as follows. An undoped $Ga_{0.25}In_{0.75}As_{0.54}P_{0.46}$ core layer ($\lambda_g = 1.25$ μm, 200-nm thick) and an undoped InP cladding layer (500-nm thick) were grown on a (100) semi-insulating InP substrate by organometallic vapor phase epitaxy (OMVPE). On the surface of the cladding layer, SRRs

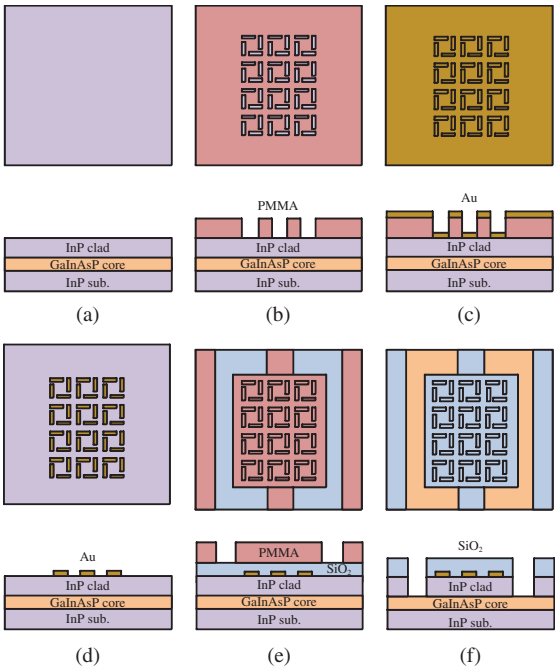

Fig. 8. Fabrication process for metamaterial MMI device. (a) Initial wafer. (b) SRR array pattern is written onto the resist by using EBL. (c) 5-nm thick Ti and a 20-nm thick Au are deposited. (d) Unexposed resist is removed along with the metal on top during lift-off with acetone. (e) After a 75-nm-thick SiO_2 film is deposited on the wafer, EBL is used to write a 1×1 MMI pattern onto the resist. (f) Exposed regions of the SiO2 film and InP cladding layer are etched by using buffered HF and RIE, respectively.

consisting of Ti and Au layers were prepared using electron-beam lithography (EBL) and lift-off process.

The fabrication process is illustrated in Fig. 8 with both cross-sectional and plan views. The process flow was as follows: a resist layer of polymethyl methacrylate (PMMA) was first spin coated onto the InP cladding layer. Following spin coating, EBL was used to write a desired SRR array pattern onto the resist. The exposed areas of the resist were dissolved during development with xylene (Fig. 8(b)), resulting in a mask for the subsequent metal-evaporation process (Fig. 8(c)). Subsequently, the unexposed resist was removed along with the metal on top during lift-off with acetone (Fig. 8(d)). Figure 9 shows oblique scanning electron microscope (SEM) images of the *4-cut* SRR array fabricated according to this procedure. The SRRs were made of 5-nm-thick titanium and 20-nm-thick gold, and the dimensions of the individual SRR were determined on the basis of the simulation results shown in Fig. 4 ($L = 750$ nm, $W_1 = 100$ nm, $W_2 = 100$ nm, $d = 1.6$ μm). We used a 25-nm metal layer for simplicity in device fabrication (the lift-off process). Although we used 50 nm (twice the penetration depth of gold) in simulation, removing an unexposed resist layer along with such a thick metal on the resist was not easy with our experimental technique. To carry out this lift-off process successfully, we used a 25-nm metal. In addition, we chose 1.6 μm for simplicity in device fabrication. It is true that 1.5 μm is a little better than 1.6 μm for the device performance. However, with our experimental technology, a 1.6-μm SRR array can be fabricated far easily

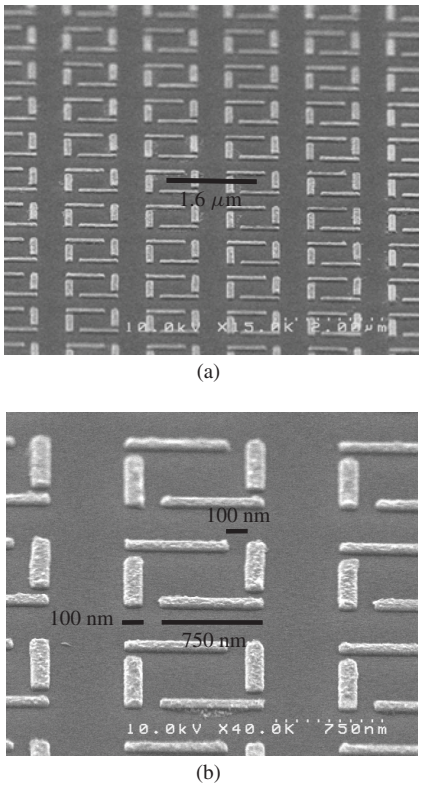

(a)

(b)

Fig. 9. Oblique views of *4-cut* SRR array, observed with scanning electron microscopy: (a) SRR array and (b) enlarged view of individual SRRs.

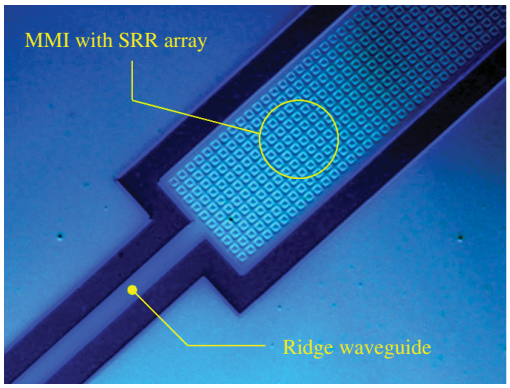

Fig. 10. Plan view of GaInAsP/InP 1×1 MMI coupler with SRR array observed with optical microscopy.

(high yield) compared with a 1.5-μm SRR array. Therefore we used 1.6 μm.

After the SRR array was formed, a 75-nm-thick SiO_2 film was deposited on the wafer by using plasma-enhanced chemical vapor deposition. Following the spin coating of PMMA, EBL was used again to write a 1×1 MMI pattern onto the resist (Fig. 8(e)). Finally, the exposed regions of the SiO_2 film and InP cladding layer were etched by using buffered HF and reactive ion etching (RIE), respectively, with a mixture gas of CH_4 and H_2 (Fig. 8(f)).

Figure 10 shows the magnified plan of the trial device observed using an optical microscope; the area around the edge of an input waveguide in the MMI coupler is shown. Three samples with different MMI lengths—630, 660, and 690 μm—were fabricated; here, the MMI width was set

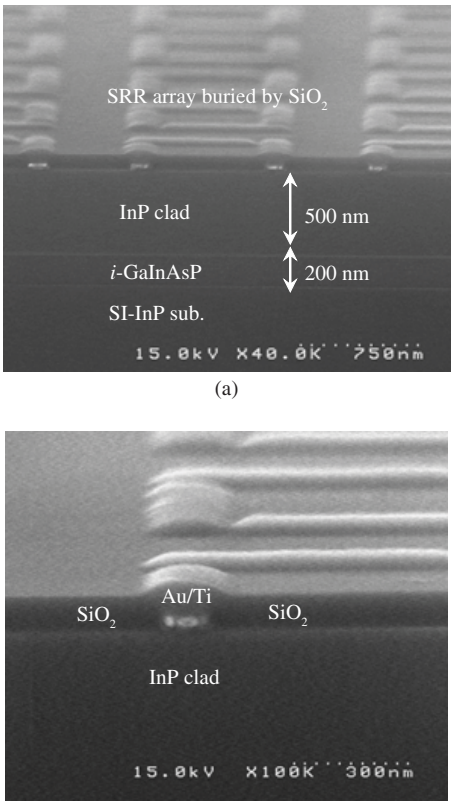

Fig. 11. SEM images of finished device, with cross-section: (a) oblique view of SRR array buried in SiO_2 layer and (b) enlarged view of individual SRRs.

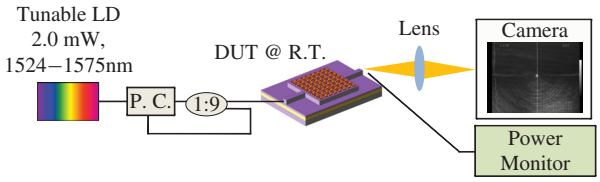

Fig. 12. Experimental setup to measure magnetic interactions in the device.

as 15 μm. Figure 11 shows oblique views of a fabricated MMI waveguide with the SRR array. The SRR array was covered entirely with an SiO_2 layer during the fabrication process, which can be observed in Fig. 11. In this study, the SiO_2 layer was not removed to prevent damages to the nanoscale SRR.

In the following optical measurements, we observe the magnetic interactions of the propagating light and SRRs in the device. To clarify this effect easily, control MMIs without SRR arrays were also prepared in addition to the abovementioned devices.

IV. Measurements and Discussion

As described in Section II, if magnetic interactions occur between the SRRs and light, the effective permeability of the SRR array becomes non-unity, i.e., large positive or negative values. At the same time, the imaginary part of the permeability increases from 0 to a finite value, and this implies that light is absorbed in the device. Since it is possible to know the occurrence of the interaction by measuring the propagation loss of light in the device, we primarily measured the transmission and absorption of light in the device.

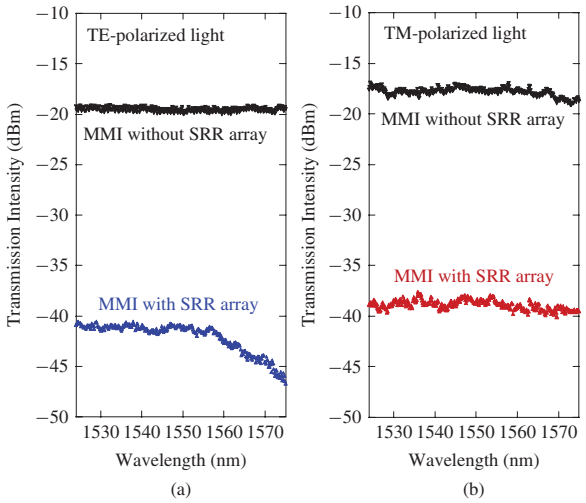

Fig. 13. Output intensity of devices with SRR (blue/red lines) and without SRRs (black lines) as a function of wavelength from 1524 to 1575 nm, measured for (a) TE mode and (b) TM mode. The length of the MMI was 660 μm.

Figure 12 shows our experimental setup for the measurements. The light source was a tunable laser with wavelength ranging from 1524 to 1575 nm. Light from the tunable laser was first passed through a polarization controller (P.C.) and then sent to one end of the device through a fiber. The output light from the other end of the device was gathered by a lens to observe a near-field pattern (see inset in Fig. 12). After confirming that the output light is in a single mode, we measured its intensity. Our device is for TE-mode operations, but for comparison, we also measured the transmission of TM-mode light. During the measurements, the device was maintained at room temperature.

Figure 13 plots the intensity of the measured output light for the experimental device with SRRs (blue/red curves) in comparison with that for the control device without SRRs (black curves), as a function of wavelength of around 1550 nm. Figures 13(a) and 13(b) show the plot for the TE-mode and TM-mode light, respectively. For the TE mode, the experimental device (with SRRs) showed gradual decrease in transmission intensity as the wavelength increased (see the blue curve). In contrast, no decrease was observed in the control device (without SRRs). For the TM mode, neither the experimental nor the control devices showed a decrease. This polarization-wavelength dependent absorption is positive proof that the magnetic interaction was successfully established in our device for the TE-mode light. In this manner, we can realize *non-unity* permeability in InP-based photonic devices by using the SRR metamaterial

Furthermore, for the TE mode, a magnetic field perpendicular to the axis of the split-ring, by virtue of Ampere's law, created a circulating current via the charge accumulation at the gap (see Section II for details). Due to the presence of gaps, the resulting charge distribution was asymmetric; this results in charge accumulation around the capacitive gaps and

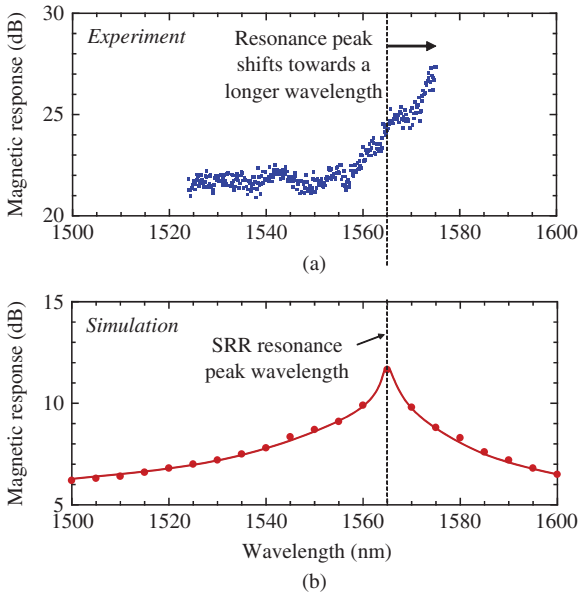

Fig. 14. Magnetic response of the transmission of TE-mode light, i.e., difference between transmission intensity of device with and without SRRs: (a) measured result and (b) calculation.

induces an electric dipole moment. On the other hand, for the TM mode, an electric field is present parallel to the two symmetric sides of the split-ring, whereas in the approximation of the thin metallization, the current in the perpendicular directions was negligible. In addition, the size of the ring was smaller than the incident wavelength, and this ensured that the variations in the electric field between the two sides were also negligible for a first approximation. Consequently, the charge distribution resulting from this incidence was symmetric and did not generate a circulating current.

The transmission data shown in Fig. 13 include unessential loss of light caused by the measurement system, such as lens-fiber coupling loss, in addition to the intrinsic losses due to the effect of the SRR array. To extract the intrinsic loss, we used the difference between the transmission intensity of the experimental device (with SRRs) and that of the control device (without SRRs). We call this difference a *magnetic response*. Figure 14(a) depicts the magnetic response of the transmission of TE-mode light.

Before discussing this result, we show in Fig. 14(b) the theoretical data for the magnetic response. The magnetic response theoretically consists of two components. One is a resonant component that increases as the wavelength approaches the resonant wavelength (1565 nm) of the SRRs. This component is a result of the essential operations of the device and shows the occurrence of successful magnetic interactions between SRRs and light. The other component is a constant (approximately 6 dB) that is independent of wavelength, and it is present due to the light absorption in the SRR metal; this component must be reduced for practical applications.

Compared with the theoretical expectations (Fig. 14(b)), the measured magnetic resonance (Fig. 14(a)) differed with respect to the following two points:

1) The measured resonant wavelength was longer than expected and exceeded 1575 nm, which is the upper limit of our tunable laser. This was probably due to the difference in the host material for the SSRs. In our theoretical calculations, we assumed that the SSRs were placed in air. However, in the actual device, the SSRs were sandwiched between an InP cladding layer and SiO_2 passivation layer. The permittivity of InP and SiO_2 is larger than that of air, and this decreases the resonance frequency of the SRR, thereby increasing the resonance wavelength.
2) The constant component was approximately 20 dB and larger than the expected value of 6 dB. The reason for this is not yet clear. One idea is that the light in the MMI might have penetrated through the cladding layer to a larger extent than expected, and therefore, it was highly absorbed in the SRR metal. This situation can be improved by readjusting the cladding layer thickness.

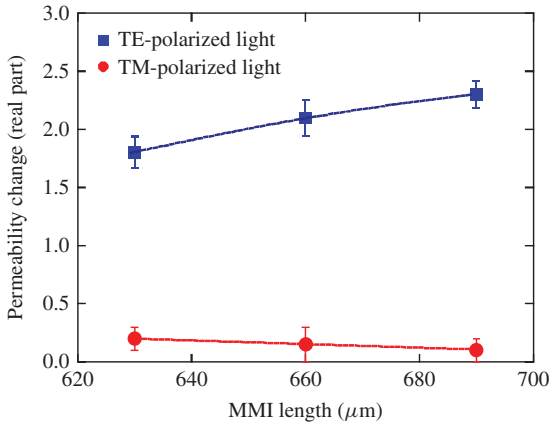

Fig. 15. Maximum change of SRR-array permeability (real part) from 1, depicted for three values of device length.

Although Fig. 14(a) is only a part of the magnetic resonance curve, we used this data to roughly estimate the effective permeability of the SRR array. For the estimation, we assumed that the SRRs resonated at 1575 nm and assumed the peak of the magnetic response at this wavelength (although the actual resonant wavelength might be longer than 1575 nm). Under this assumption, we calculated the maximum change in the permeability (real part) from 1. Figure 15 shows the results for three device lengths. The maximum calculated change are underestimated and may be larger because the magnetic response peak would be larger than shown in Fig. 14(a) if the resonant wavelength was longer than 1575 nm. In any case, we were able to confirm the feasibility of controlling the permeability in InP-based photonic devices.

Expanding a measurement-wavelength range for the device is one important element to determine the location of the resonance in Figs. 14 and 15. However, our MMI is designed for use in C band (1530–1565 nm), the operation range of erbium-doped fiber amplifiers, and cannot operate well at other wavelengths. Therefore it may be difficult to measure the magnetic response accurately at longer wavelengths.

V. Conclusion

Realizing *non-unity* permeability at optical frequencies can be expected to lead us to advanced optical-communication

devices based on novel operation principles. To move one step closer to this goal, in this paper, we have demonstrated that the permeability in semiconductor photonic devices can be controlled using the concept of metamaterials.

As an actual example, we fabricated a GaInAsP/InP MMI device combined with an SRR array that operated as a metamaterial layer. The operation wavelength was set as 1.55 μm. The transmission characteristics of this metamaterial MMI device strongly depended on the polarization and wavelength of input light. This shows that the SRR array layer interacted with the magnetic field of light and produced magnetic resonance at optical frequencies. In this manner, we have been able to demonstrate magnetic interactions between the metamaterial and light traveling in the MMI. Our results show the feasibility of semiconductor-based photonic devices combined with metamaterials. This would be useful in the development of novel optical-communication devices.

REFERENCES

[1] R. M. Walser, "Electromagnetic metamaterials," *Proc. SPIE*, vol. 4467, pp. 1–15, Jul. 2001.

[2] H. J. Lezec, J. A. Dionne, and H. A. Atwater, "Negative refraction at visible frequencies," *Science*, vol. 316, no. 5823, pp. 430–432, Mar. 2007.

[3] W. Cai, U. K. Chettiar, H. K. Yuan, V. C. de Silva, A. V. Kildishev, V. P. Drachev, and V. M. Shalaev, "Metamagnetics with rainbow colors," *Opt. Exp.*, vol. 15, no. 6, pp. 3333–3341, Mar. 2007.

[4] J. Valentine, S. Zhang, T. Zentgraf, E. Ulin-Avila1, D. A. Genov1, G. Bartal1, and X. Zhang, "3-D optical metamaterial with a negative refractive index," *Nature*, vol. 455, no. 7211, pp. 376–379, Aug. 2008.

[5] R. Nagarajan, C. H. Joyner, R. P. Schneider, Jr., J. S. Bostak, T. Butrie, A. G. Dentai, V. G. Dominic, P. W. Evans, M. Kato, M. Kauffman, D. J. H. Lambert, S. K. Mathis, A. Mathur, R. H. Miles, M. L. Mitchell, M. J. Missey, S. Murthy, A. C. Nilsson, F. H. Peters, S. C. Pennypacker, J. L. Pleumeekers, R. A. Salvatore, R. K. Schlenker, R. B. Taylor, H. S. Tsai, M. F. V. Leeuwen, J. Webjorn, M. Ziari, D. Perkins, J. Singh, S. G. Grubb, M. S. Reffle, D. G. Mehuys, F. A. Kish, and D. F. Welch, "Large-scale photonic integrated circuits," *IEEE J. Sel. Topics Quantum Electron.*, vol. 11, no. 1, pp. 50–65, Feb. 2005.

[6] J. V. Campenhout, P. R. Romeo, P. Regreny, C. Seassal, D. V. Thourhout, S. Verstuyft, L. D. Cioccio, J.-M. Fedeli, C. Lagahe, and R. Baets, "Electrically pumped InP-based microdisk lasers integrated with a nanophotonic silicon-on-insulator waveguide circuit," *Opt. Exp.*, vol. 15, no. 11, pp. 6744–6749, Mar. 2007.

[7] M. J. R. Heck, P. Muñoz, B. W. Tilma, E. A. J. M. Bente, Y. Barbarin, Y. S. Oei, R. Nötzel, and M. K. Smit, "Design, fabrication and characterization of an InP-based tunable integrated optical pulse shaper," *IEEE J. Quantum Electron.*, vol. 44, no. 4, pp. 370–377, Apr. 2008.

[8] S. C. Nicholes, M. L. Masanovic, B. Jevremovic, E. Lively, L. A. Coldren, and D. J. Blumenthal, "The world's first InP 8×8 monolithic tunable optical router (MOTOR) operating at 40 Gb/s line rate per port," in *Proc. Opt. Fiber Commun. Conf.*, San Diego, CA, 2009, pp. 1–3.

[9] C. R. Doerr, L. Zhang, and P. J. Winzer, "Monolithic InP multiwavelength coherent receiver," in *Proc. Opt. Fiber Commun. Conf.*, San Diego, CA, Mar. 2010, no. PDPB1, pp. 1–3.

[10] J. J. G. M. van der Tol, Y. S. Oei, U. Khalique, R. Nötzel, and M. K. Smit, "InP-based photonic circuits: Comparison of monolithic integration techniques (review paper)," *Prog. Quantum Electron.*, vol. 34, no. 4, pp. 135–172, Jul. 2010.

[11] I. V. Shadrivov, A. A. Sukhorukov, and Y. S. Kivshar, "Guided modes in negative-refractive-index waveguides," *Phys. Rev. E*, vol. 67, no. 5, pp. 057602-1–057602-4, May 2003.

[12] A. Peacock and N. Broaderick, "Guided modes in channel waveguides with a negative index of refraction," *Opt. Exp.*, vol. 11, no. 20, pp. 2502–2510, Oct. 2003.

[13] K. L. Tsakmakidis, A. D. Boardman, and O. Hess, "Trapped rainbow storage of light in metamaterials," *Nature*, vol. 450, no. 7168, pp. 397–401, Nov. 2007.

[14] A. Figotin and I. Vitebskiy, "Slow-wave resonance in periodic stacks of anisotropic layers," *Phys. Rev. A*, vol. 76, no. 5, pp. 053839-1–053839-12, May 2007.

[15] K.-Y. Jung, F. L. Teixeira, and R. M. Reano, "Au/SiO_2 nanoring plasmon waveguides at optical communication band," *IEEE J. Lightwave Technol.*, vol. 25, no. 9, pp. 2757–2765, Sep. 2007.

[16] K.-Y. Jung and F. L. Teixeira, "Photonic crystals with a degenerate band edge: Field enhancement effects and sensitivity analysis," *Phys. Rev. B*, vol. 77, no. 12, pp. 125108-1–125108-9, Dec. 2008.

[17] T. J. Yen, W. J. Padilla, N. Fang, D. C. Vier, D. R. Smith, J. B. Pendry, D. N. Basov, and X. Zhang, "Terahertz magnetic response from artificial materials," *Science*, vol. 303, no. 5663, pp. 1494–1496, Mar. 2004.

[18] S. Zhang, W. Fan, B. K. Minhas, A. Frauenglass, K. J. Malloy, and S. R. J. Brueck, "Midinfrared resonant magnetic nanostructures exhibiting a negative permeability," *Phys. Rev. Lett.*, vol. 94, no. 3, pp. 037402-1–037402-4, Jan. 2005.

[19] C. Enkrich, M. Wegener, S. Linden, S. Burger, L. Zschiedrich, F. Schmidt, J. F. Zhou, T. Koschny, and C. M. Soukoulis, "Magnetic metamaterials at telecommunication and visible frequencies," *Phys. Rev. Lett.*, vol. 95, no. 20, pp. 203901-1–203901-4, Nov. 2005.

[20] S. Linden, C. Enkrich, G. Dolling, M. W. Klein, J. Zhou, T. Koschny, C. M. Soukoulis, S. Burger, F. Schmidt, and M. Wegener, "Photonic metamaterials: Magnetism at optical frequencies," *IEEE J. Sel. Topics Quantum Electron.*, vol. 12, no. 6, pp. 1097–1105, Dec. 2006.

[21] C. E. Kriegler, M. S. Rill, S. Linden, and M. Wegener, "Bianisotropic photonic metamaterials," *IEEE J. Sel. Topics Quantum Electron.*, vol. 16, no. 2, pp. 367–375, Mar. 2010.

[22] S. Ramo, J. R. Whinnery, and T. V. Duzer, *Field and Waves in Communication Electronics*. New York: Wiley, 1993, pp. 149–156.

[23] A. Ishikawa, T. Tanaka, and S. Kawata, "Frequency dependence of the magnetic response of split-ring resonators," *J. Opt. Soc. Amer. B*, vol. 24, no. 3, pp. 510–515, Mar. 2007.

[24] S. A. Ramakrishna, "Physics of negative refractive index materials," *Rep. Prog. Phys.*, vol. 68, no. 2, pp. 449–521, Jan. 2005.

[25] A. Ishikawa, T. Tanaka, and S. Kawata, "Negative magnetic permeability in the visible light region," *Phys. Rev. Lett.*, vol. 95, no. 23, pp. 237401-1–237401-4, Dec. 2005.

[26] D. R. Smith and J. B. Pendry, "Homogenization of metamaterials by field averaging (invited paper)," *J. Opt. Soc. Amer. B*, vol. 23, no. 3, pp. 391–403, Mar. 2006.

[27] L. B. Soldano and E. C. M. Pennings, "Optical multi-mode interference devices based on self-imaging: Principles and applications," *IEEE J. Lightwave Technol.*, vol. 13, no. 4, pp. 615–627, Apr. 1995.

Tomohiro Amemiya (S'06–M'09) received the B.S., M.S., and Ph.D. degrees in electronic engineering from the University of Tokyo, Tokyo, Japan, in 2004, 2006, and 2009, respectively.

He joined the Quantum Electronics Research Center, Tokyo Institute of Technology, Tokyo, in 2009, where he is currently an Assistant Professor. His current research interests include physics of semiconductor light-controlling devices, metamaterials for optical frequency, magnetooptical devices, and processing technologies for fabricating these devices.

Dr. Amemiya is a member of the Optical Society of America, the American Physical Society, and the Japan Society of Applied Physics. He was the recipient of the IEEE Photonics Society Annual Student Paper Award in 2007 and the IEEE Photonics Society Graduate Student Fellowships in 2008.

Takahiko Shindo (S'10) received the B.E. and M.E. degrees in electrical and electronic engineering from the Tokyo Institute of Technology, Tokyo, Japan, in 2007 and 2009, respectively. He is currently pursuing the Ph.D. degree at the Quantum Electronics Research Center, Tokyo Institute of Technology.

He has been working as a Research Fellow of the Japan Society for the Promotion of Science, Japan, since 2010. His current research interests include photonic integrated devices on a silicon platform.

Mr. Shindo is a Student Member of the Japan Society of Applied Physics.

Daisuke Takahashi received the B.E. degree in electrical and electronic engineering from the Tokyo Institute of Technology, Tokyo, Japan, in 2008. He is currently pursuing the M.E. degree.

His current research interests include studies on low-damage and cost-effective processing technologies of ultrafine structures for high-performance lasers.

Mr. Takahashi is a Student Member of the Japan Society of Applied Physics.

Nobuhiko Nishiyama (M'01–SM'07) was born in Yamaguchi, Japan, in 1974. He received the B.E., M.E., and Ph.D. degrees from the Tokyo Institute of Technology, Tokyo, Japan, in 1997, 1999, and 2001, respectively. During his Ph.D. work, he demonstrated single-mode 0.98- and 1.1-μm vertical-cavity surface-emitting laser (VCSEL) arrays with stable polarization using misoriented substrates for high-speed optical networks as well as GaInNAs VCSELs grown by metal-organic chemical vapor deposition.

He joined the Semiconductor Technology Research Group, Corning Inc., Corning, NY, in 2001. At Corning, he worked on several subjects including short-wavelength lasers, 1060-nm DFB/DBR lasers, and long-wavelength InP-based VCSELs, demonstrating state-of-the-art results such as 10-Gbit/s isolator-free and high-temperature operations of long-wavelength VCSELs. Since 2006, he has been an Associate Professor at the Tokyo Institute of Technology. His current research interests include laser transistors, silicon photonics, III–V silicon hybrid optical devices, and terahertz optical signal conversions involving optics-electronics-radio integrated circuits.

Dr. Nishiyama is a member of the Japan Society of Applied Physics, the Institute of Electronics, Information and Communication Engineers (IEICE), Japan, and the IEEE Photonics Society. He received an Excellent Paper Award from the IEICE in 2001 and the Young Scientists Prize in the Commendation for Science and Technology from the Minister of Education, Culture, Sports, Science and Technology, Japan, in 2009.

Shigehisa Arai (M'83–SM'06–F'10) received the B.E., M.E., and D.E. degrees in electronics from the Tokyo Institute of Technology, Tokyo, Japan, in 1977, 1979, and 1982, respectively.

He joined the Department of Physical Electronics, Tokyo Institute of Technology, as an Assistant Professor in 1982, where he became an Associate Professor in 1987 and a Professor with the Research Center for the Quantum Effect Electronics in 1994. From 1983 to 1984, he was with AT&T Bell Laboratories, Holmdel, NJ. Since 2004, he has been a Professor with the Quantum Nanoelectronics Research Center, Tokyo Institute of Technology. He is also with the Department of Electrical and Electronic Engineering, Tokyo Institute of Technology. His current research interests include photonic integrated devices such as dynamic single-mode and wavelength-tunable semiconductor lasers, semiconductor optical amplifiers, and optical switches/modulators, studies on low-damage and cost-effective processing technologies of ultrafine structures for high-performance lasers, and photonic integrated circuits on silicon platforms.

Dr. Arai is a member of the Optical Society of America, the Institute of Electronics, Information and Communication Engineers (IEICE), Japan, and the Japan Society of Applied Physics (JSAP). He received an Excellent Paper Award from the IEICE in 1988, the Michael Lunn Memorial Award from the Indium Phosphide and Related Materials Conference in 2000, Prizes for Science and Technology including a Commendation for Science and Technology from the Minister of Education, Culture, Sports, Science and Technology in 2008, an Electronics Society Award from IEICE in 2008, and a JSAP Fellowship in 2008.